Alpha Research, Inc.
Report No. 67-3426-1
27 March 1967

N67-22882

# NON-LINEAR AERODYNAMIC NORMAL FORCE AND MOMENT ON SLENDER BLUNT-BASED BODIES OF REVOLUTION WITH LAMINAR BOUNDARY LAYER

FACILITY FORM 602

34 (PAGES)

(NASA CR OR TMX OR AD NUMBER)

(THRU) 0

(CODE) 01

(CATEGORY)

by

Ray W. Rodman
Consultant

prepared for

NASA Ames Research Center
Moffett Field, California

Contract NAS 2-3426

REPRODUCED BY
NATIONAL TECHNICAL
INFORMATION SERVICE
U.S. DEPARTMENT OF COMMERCE
SPRINGFIELD, VA. 22161

N O T I C E

THIS DOCUMENT HAS BEEN REPRODUCED FROM THE BEST COPY FURNISHED US BY THE SPONSORING AGENCY. ALTHOUGH IT IS RECOGNIZED THAT CERTAIN PORTIONS ARE ILLEGIBLE, IT IS BEING RELEASED IN THE INTEREST OF MAKING AVAILABLE AS MUCH INFORMATION AS POSSIBLE.

October 2, 1966

# Non - Linear Aerodynamic Normal Force And Moment On Slender Blunt - Based Bodies of Revolution With Laminar Boundary Layer.

By Ray W. Rodman

## Summary

A method based on revised crossflow concepts is presented for the estimation of the non-linear normal force and moment on slender, blunt-based bodies of revolution. The method is applicable to both subsonic and supersonic flows, and covers the angle of attack range of zero to ninety degrees. Comparisons with experimental normal force distributions show that the correct form of the longitudinal normal force distribution is provided by the method. The method is strictly applicable only to the case of a fully laminar boundary layer over the entire body length. However, some effects of boundary layer transition are pointed out. Since the turbulent crossflow drag coefficient is strongly a function of angle of attack, an essential difference exists between laminar and turbulent crossflow separation over bodies of revolution. The implications of this basic difference on the initial longitudinal development of turbulent crossflow separation have not as yet been established.

## Introduction

Available analytical methods for the estimation of normal force and pitching moment coefficients of bodies of revolution at moderately low to high angles of attack are generally quite inaccurate and lacking in generality. Newtonian Theory, which is accurate for slender nose regions of bodies over a limited high Mach number/angle of attack range, is of little use for bodies with long, cylindrical afterbodies. The only other available non-linear theory is the crossflow theory of Allen (1). However, the crossflow concept has not been highly developed and normal force distributions calculated with two widely used applications of the method (1)(2) tend to differ considerably from experimental results (3), (4).

A development of the crossflow theory which gives generally more favorable agreement with experiment than either (1) or (2) is presented herein.

## Symbols and Nomenclature

$(C_{d_c})_{2-D}$ steady state crossflow drag coefficient of an element of an infinite cylinder, based on element planform area.

$C_{dc}$ local crossflow drag coefficient of an element of a body of revolution, based on element planform area.

$c_{n_v}$ viscous crossflow separation contribution to local normal force coefficient, per calibre of body length, with one calibre equal to one reference diameter of body length.

$c_{n_p}$ potential flow contribution to local normal force coefficient, per calibre of body length.

$C_N$ body normal force coefficient

$C_m$ body pitching moment coefficient

$d$ local body diameter, feet

$d_b$ base diameter, feet

$d_c$ cylinder diameter, feet

$d_{ref}$ reference diameter, feet

$F_N$ local body viscous cross force, pounds

$\ell$ body length, feet

$\ell_e$ an effective body length used in estimating the parameter $k_2$, feet

$\ell_N$ nose length, feet

$r$ local body radius, feet

$d_M$ body dia. at station $X_M$

$M_\infty$ free stream Mach number

$M_c$ crossflow Mach number

$q_c$ crossflow dynamic pressure, pounds per square foot

$t$ time, seconds

| | |
|---|---|
| $K_1$ | parameter used in impulsive flow analogy to correct for influence of potential flow normal force distribution on viscous cross-flow separation |
| $K_2$ | correction factor to normal force and pitching moment coefficients due to body base effect |
| $S_p$ | Planform area of body, square feet |
| $S_{ref}$ | reference area , square feet |
| $V_c$ | crossflow velocity, feet per second |
| $V_\infty$ | free stream velocity, feet per second |
| $X$ | axial station measured aft from vertex of body nose, feet |
| $X_s$ | axial station at which crossflow separation commences, feet |
| $X_M$ | axial station at which the potential flow contribution to the local normal force coefficient reaches a minimum. |
| $X_{mc}$ | axial station about which pitching moment coefficient is taken |
| $X_1$ | in subsonic flows, the axial station at which the rate of change of body cross section area with axial distance along the body reaches a maximum negative value. |

Greek Symbols

| | |
|---|---|
| $\rho$ | air density, slugs per cubic ft. |
| $\alpha$ | angle of attack |
| $\alpha_s$ | angle of attack at which crossflow separation first begins at nose vertex |
| $\theta_v$ | nose vertex half angle |

Subscripts:

| | |
|---|---|
| $\infty$ | free stream value |
| $c$ | crossflow value or cylinder |
| $v$ | viscous crossflow contribution or nose vertex |
| $p$ | potential flow contribution |

## Discussion

### A. GENERAL

Since the introduction of the crossflow theory by Allen (1) for the estimation of non-linear aerodynamic forces and moments, refinements to the basic concept have been proposed (2) which purportedly produce results in better agreement with experiment than the original theory. However, subsequent investigations (3), (4) have shown that neither Allen's nor Kelly's results accurately predict the normal force distributions of slender bodies of revolution. Allen's original method is grossly in error in the nose region of most bodies, while Kelly's formulation overestimates crossflow drag over cylindrical portions of bodies far downstream of the nose. In addition, Kelly's method does not produce correct longitudinal normal force distributions for the limiting case as angle of attack approaches ninety degrees. Neither method adequately accounts for a turbulent boundary layer condition, since both methods use a turbulent crossflow drag coefficient of 0.35 at low angles of attack. The turbulent steady state crossflow drag coefficient has, however, been shown to be a strong function of angle of attack (5), approaching a value of approximately 0.8 at low alpha.

The method presented herein utilizes a form of the laminar impulsive flow analogy, suitably modified to account for the influence of nose shape and Mach number, to establish the longitudinal distribution of crossflow drag coefficient. The basic form of the laminar impulsive crossflow drag coefficient is obtained from the experimental results of Sarpkaya (6). Utilization of a laminar impulsive flow parameter is such that the correct crossflow drag coefficient results in the limiting case of ninety degrees angle of attack (body broadside to wind).

A basic assumption of both Allen and Kelly is that crossflow separation starts at the vertex of the body nose, even at very low angles of attack.

This assumption is obviously unrealistic and a revised criterion for the commencement of crossflow separation, placing that position downstream of the nose vertex at low angles of attack, is presented herein. The results of references 4 and 7 ( for supersonic and subsonic flows respectively) are utilized to establish reference locations on the body to associate with the maximum value of the impulsive laminar crossflow drag coefficient parameter. Longitudinal distributions of crossflow drag coefficient over the body are consequently determined as functions of angle of attack, for the prescribed body configuration and free stream conditions.

## Discussion

### B. REVIEW OF CROSSFLOW THEORY

Allen's crossflow theory (1) states that the local viscous cross force ( force per unit of cylinder length in units of cylinder diameter) over an infinite cylinder can be expressed in terms of a crossflow drag coefficient which depends on a dynamic pressure based on the cross-velocity component, and the planform area of the cylinder. This relationship can be expressed as ( Figure 1)

$$(1)\quad (C_{dc})_{2\text{-}D} = \frac{d F_N}{d q_c\, dx} \quad \text{or} \quad \frac{d F_N}{dx} = d\, q_c (C_{dc})_{2\text{-}D}$$

where $d$ is the local body diameter and where

$$(2)\quad q_c = \frac{\rho_\infty V_c^2}{2} = \frac{\rho_\infty}{2}\left(V_\infty \sin\alpha\right)^2$$

The local viscous crossforce ( force per unit of cylinder length) can be appropriately termed the local viscous normal force ( 2 ). A local viscous normal force coefficient based on free stream dynamic pressure and an arbitrary reference area, $S_{ref}$, (usually taken as the body maximum cross section area) can then be defined as

$$(3) \quad C_{n_v} = \frac{dF_N}{d\left(\frac{x}{d_{ref}}\right)} \frac{1}{q_\infty S_{ref}} = \frac{dF_N}{dx} \frac{d_{ref}}{q_\infty S_{ref}}$$

where the units on $C_{n_v}$ are "per calibre of body length", with one calibre equal to the diameter of the circular reference area, $d_{ref}$, as given below:

$$(4) \quad d_{ref} = \left(\frac{4 S_{ref}}{\pi}\right)^{1/2}$$

combining (1),(2),(3) and (4) we have

$$(5) \quad C_{n_v} = \frac{4d}{\pi d_{ref}} C_{d_c} \sin^2\alpha$$

For a body of finite length equation (5) can be integrated to produce the viscous contribution to body normal force and pitching moment coefficients.

It was originally noted by Allen (1) that for finite length bodies an adjustment of the two-dimensional crossflow drag coefficient was required. Allen proposed a correction factor based on body length-to-diameter ratio to account for this influence. A more refined analysis of the axial development of crossflow separation was later developed by Kelly (2), which afforded a more accurate estimate of viscous cross force in the nose region of a slender body. Kelly's analysis, however, assumed that viscous separation commenced at the body nose and induced a crossflow drag coefficient which increased continuously over the body length in a manner completely analagous to the timewise variation of laminar impulsive drag over a circular cylinder, as obtained by Schwabe (8).

Subsequent data have shown that crossflow separation does not generally start at the body nose (3),(4) and that the crossflow drag coefficient does not increase indefinitely in the laminar impulsive cylinder drag analogy (9). These findings are included in the development which follows.

Assuming that crossflow separation begins at some axial station downstream of the body nose (defined as station $X_s$), the appropriate equations for the viscous normal force and moment coefficients obtained by integrating equation (5) are

$$(6) \quad C_{N_V} = k_2 \frac{d_{ref} \sin^2\alpha}{S_{ref}} \int_{\frac{X_s}{d_{ref}}}^{\frac{\ell}{d_{ref}}} d C_{dc} \, d\left(\frac{X}{d_{ref}}\right)$$

$$(7) \quad C_{m_V} = k_2 \frac{d_{ref} \sin^2\alpha}{S_{ref}} \int_{\frac{X_s}{d_{ref}}}^{\frac{\ell}{d_{ref}}} d C_{dc} \left(\frac{X_{mc} - X}{d_{ref}}\right) d\left(\frac{X}{d_{ref}}\right)$$

The factor $k_2$ introduced in equations 6 and 7 is used here as a correction factor to account for the influence of the body base on the overall magnitude of the crossflow drag coefficient. This effect will be discussed in a separate section which follows. The effect of the factor $k_2$ will be seen to be significant only at subsonic speeds, where the base flow distortion influences the crossflow upstream of the base.

Each parameter which appears in equations 6 and 7 will now be discussed under a separate section, and methods for estimating these individual parameters as functions of Mach number, body geometry, angle of attack, and boundary layer condition will be presented.

## C. The Crossflow Drag Coefficient, $C_{dc}$

### C - 1 The Impulsive Flow Analogy

Similarity of the axial development of the crossflow drag coefficient over a body of revolution with a totally laminar boundary layer to the impulsive laminar flow about a cylinder has been well established (2). Strict application of the analogy requires that time in the impulsive flow be replaced by axial progression of the flow along the body of revolution. Thus if crossflow separation on a body of revolution starts at the axial station $X_s$, then a station downstream of $X_s$, denoted by $X$, has a crossflow drag coefficient obtained from the impulsive laminar parameter at a time given by equation 8.

$$(8) \quad \frac{V_c t}{d} = \frac{(X - X_s)}{d} \tan \alpha$$

A plot of experimental, incompressible crossflow drag coefficient versus the time dependent parameter $\frac{V_c t}{d}$ for impulsive laminar flow over a cylinder is shown in figure 2, as obtained from reference 9. It will be noted that the crossflow drag coefficient in figure 2 has been normalized against its steady state value at $t = \infty$.

The data of figure 2 were obtained for much higher values of the parameter $\frac{V_c t}{d}$ than the previous work of Schwabe, showing that the crossflow drag coefficient does indeed gradually approach the steady state value of approximately 1.2 $(M_\infty \ll 1)$.

Use of the data of figure 2 strictly according to the analogy proposed in equation 8 has been shown to produce crossflow drag distributions on bodies of revolution which are not in good agreement with experiment (3),(4). Apparently longitudinal pressure gradients due to nose shape and Mach number significantly affect the applicability of the laminar, incompressible impulsive flow analogy.

## C - 2 Revised Form of Impulsive Flow Analogy

A simple adjustment of the impulsive flow analogy to account for Mach number and nose shape influences on the axial distribution of crossflow drag coefficient on a body of revolution can be made by re-writing equation 8 as

$$(9) \quad \frac{V_c t}{d} = k_1 \frac{(x - x_s)}{d} \tan\alpha$$

The factor $k_1$ can be established as a function of angle of attack for any body by an independent determination of the locations of the start of crossflow separation (station $X_s$), and axial location at which the crossflow drag coefficient reaches a maximum (station $X_M$ shown on figure 2). Knowing these two locations the value of $k_1$, can be determined from the relation

$$(10) \quad k_1 = \frac{4.5 \frac{d_M}{d_{ref}}}{\frac{(X_M - X_s)}{d_{ref}} \tan\alpha}$$

It will be noted from figure 2 that the crossflow drag coefficient reaches a maximum at a value of the crossflow drag parameter equal to 4.5; hence the factor 4.5 appears in equation 10 for the determination of the parameter $k_1$. For a specified angle of attack, $k_1$ becomes a function only of the axial location of crossflow separation, $X_s$, and the location on the body at which the crossflow drag coefficient reaches a maximum, $X_M$, along with the body diameter($d_M$) at the station $X_M$.

Previous investigations have assumed that crossflow separation begins at the vertex of the body nose (1),(2). It is known, however, that crossflow separation on a slender body generally begins some distance downstream of the nose, progressing forward along the body as angle of attack increases. Since the location of initial (*low* $\alpha$ ) crossflow separation is a complex function of Mach number, Reynolds number,

boundary layer transition location (if present), as well as body geometry and surface condition, an accurate determination of the station $X_s$ at low angle of attack is not presently feasible. As a first approximation to this location it is suggested that the body station at which the surface slope just equals the angle of attack be used as the station $X_s$. This relation is expressed as

$$(11)\quad \left(\frac{dr}{dx}\right)_{x=X_s} = \alpha$$

Use of equation (11) for the determination of $X_s$ as a function of $\alpha$ will generally place $X_s$ farther upstream than the actual position of initial crossflow separation. However, equation 11 is most certainly a better approximation than the nose vertex as the location of the start of crossflow separation for convex nose shapes.

For cone-cylinder body configurations equation 11 places the start of crossflow separation at the cone-cylinder juncture for angles of attack less than the cone half angle. When the angle of attack reaches a value equal to the cone half angle separation moves to the vertex of the cone, according to equation 11. This effect suddenly increases the normal force as the angle of attack reaches a value equal to the cone half angle. In reality the point at which crossflow begins to separate moves upstream along the cone in a continuous manner which depends upon the boundary layer condition along the cone. Therefore, results obtained using equation 11 should be faired smoothly when plotted versus angle of attack.

The position along the body at which the crossflow distribution reaches a maximum (position $X_M$) can be physically associated with the farthest upstream position at which crossflow separation has progressed to the region of the side meridian of the body (figure 3).

FIGURE 3
CROSSFLOW VORTEX DEVELOPMENT

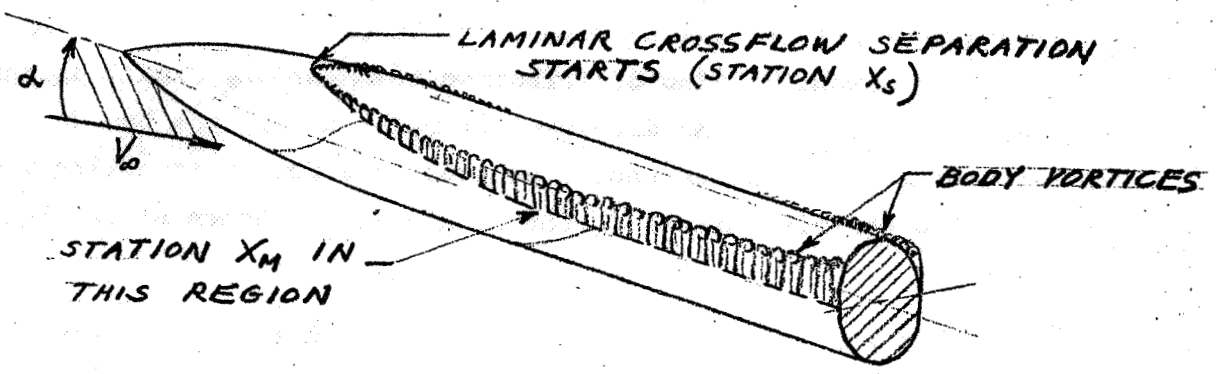


In supersonic flows position $X_M$ has been shown to be closely associated with the location on the body at which the axial distribution of the potential contribution to the normal force reaches a minimum (4). This relationship is given by the expression

$$(12) \quad \left[\frac{d\,C_{np}}{d\left(\frac{X}{d_{ref}}\right)}\right]_{\substack{X=X_M \\ X>\ell_N}} = 0$$

Figure 4 illustrates the location of $X_M$ given by equation 12.

FIGURE 4
LOCATION OF STATION $X_M$ IN SUPERSONIC FLOW

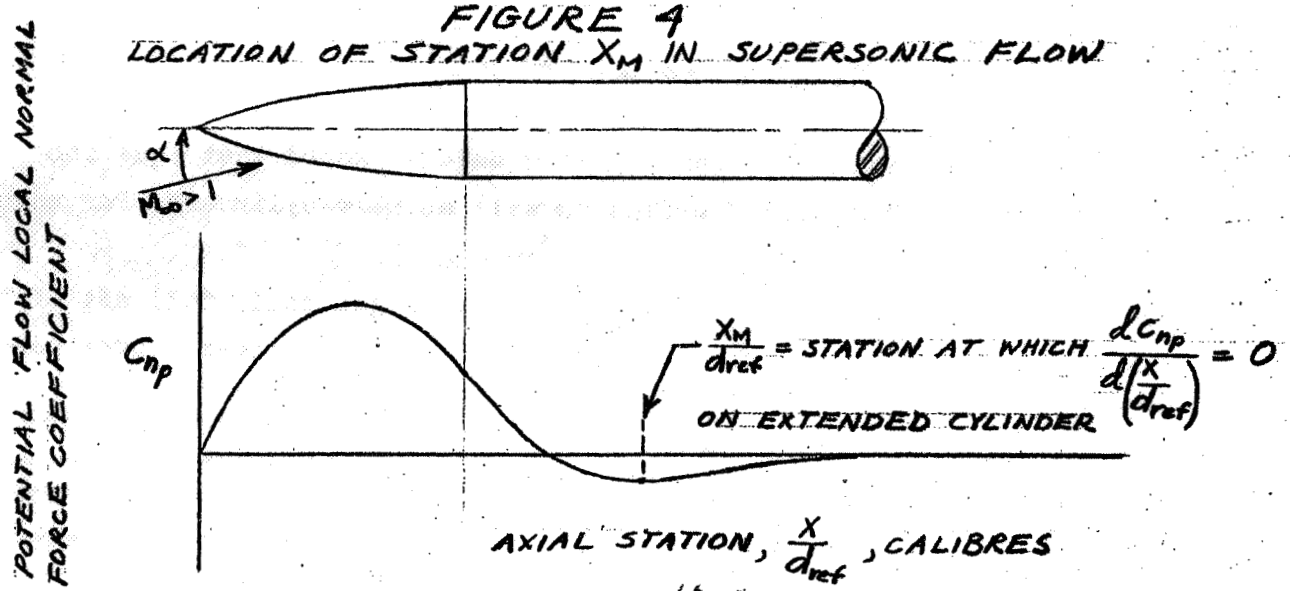

The location of station $X_M$ for supersonic flows can be obtained indirectly thru the theoretical methods of references 10 or 11 which permit estimation of the potential flow contribution to $C_{m_\alpha}$ and $C_{m_{\dot{\alpha}}}$ distributions on bodies of revolution.( As discussed in reference 2, the boundary layer displacement thickness should be accounted for in computing the potential flow contribution to $C_n$ for slender-body shapes at low Reynolds numbers).

For slender, pointed nose-cylinder combinations a rapid, approximate estimate of the location of station $X_M$ can be obtained using figure 5. The data used in developing figure 5 were taken from reference 15 .

For subsonic flows over bodies of revolution the position $X_M$ has been correlated in reference 12 as a function of the position at which the rate of change of body cross section area with axial distance has a maximum negative value ( defined as station $X_1$ ). This correlation is given by the expression

$$(13) \qquad \frac{X_M}{\ell} = 0.378 + 0.527 \frac{X_1}{\ell}$$

where $\ell$ is the total body length. It should be noted that equation (13) applies to boattailed bodies as well as nose-cylinders. For nose-cylinders it will be noted that $\frac{X_M}{\ell} = 0.905$.
The position of $X_M$ in subsonic flow will thus generally fall aft of the location of $X_M$ in a low supersonic flow, for long, nose-cylinder configurations.

As angle of attack is increased and the station at which crossflow separation first occurs (station $X_s$) moves upstream, finally reaching the vertex of the nose ( assuming the nose is pointed), the body begins to assume a more two-dimensional crossflow distribution. Though detailed experimental normal force distributions are not available for this condition, it is conjectured that the position $X_M$ gradually moves upstream after $X_s$ reaches the vertex of the nose, finally producing a two-dimensional normal force distribution over the body as a high angle of attack is attained. This trend can be analytically modeled by holding the factor $k_1$ of equation 9 constant, at angles of attack above that at which $X_s$ first reaches the vertex of the nose. This is expressed formally using equation 10 as follows

$$(14) \quad \left(k_1\right)_{\alpha \geq \theta_v} = \text{CONSTANT} = \frac{4.5 \frac{d_M}{d_{ref}}}{\frac{X_M}{d_{ref}} \tan \theta_v}$$

where $\theta_v$ is the nose-vertex half-angle. Thus, once crossflow separation reaches the vertex of the body nose, the factor $k_1$ is assumed to be constant and equal to the value given by equation 14. This assumption produces a proper distribution of crossflow drag coefficient in the limiting condition of ninety degrees angle of attack.

## C - 3 The Steady State Laminar Crossflow Drag Coefficient

Figure 2 shows the ratio of the transient crossflow drag coefficient of a circular cylinder to its steady state value. It is thus necessary to establish the value of the steady state laminar crossflow drag coefficient for use with figure 2 in any particular application.

The steady state laminar crossflow drag coefficient has been shown to be a function of crossflow Mach number, $M_c$, where

$$(15) \quad M_c = M_\infty \sin\alpha$$

Though many investigations have assumed that the crossflow drag coefficient should correlate versus crossflow Mach number regardless of whether the free stream Mach number is subsonic or supersonic, this is not a necessarily valid assumption. A more reasonable assumption is that separate crossflow drag coefficient correlations exist, one for subsonic free streams and another for supersonic free stream Mach numbers. Such correlations are shown in figure 6. The data for figure 6 were taken from references for which the flows could reasonably be expected to be totally laminar.

The subsonic free stream data shown in figure 6 were taken from reference 13, which also showed reasonably good agreement with subsonic data of reference 12. The subsonic free stream data shown are for Reynolds numbers below the critical value of approximately $2\ (10)^5$ (based on free stream conditions and body diameter). At Reynolds numbers greater than $2\ (10)^5$, a sharp decrease in crossflow drag coefficient occurs at crossflow Mach numbers below approximately 0.4 (for subsonic free streams only (12) ).

Crossflow drag coefficient data for supersonic free streams are observed to correlate well with the subsonic data up to a crossflow Mach number of approximately 0.4 . Above this crossflow Mach number,

however, the supersonic data increases in magnitude continuously, and does not display the characteristic "dip" of the subsonic free stream data. After reaching a maximum in the vicinity of a Mach one crossflow, the supersonic crossflow drag coefficient decreases continuously with increasing supersonic cross Mach number to a level approaching the low subsonic data of 1.2 .

For the cross Mach number range of approximately 1.4 to 10 the curve shown in figure 6 was a fairing thru data obtained from references 1,12 and 14. In the subsonic range of crossflow Mach number with a supersonic free stream, the data of reference 3 is shown. This data was obtained by extracting crossflow drag coefficients required to satisfy the experimental local normal force coefficient levels given in figure 9 of reference 3. The boundary layer for this data appeared to be definitely laminar, and the long, cylindrical body utilized permitted achievment of $\overset{a}{\wedge}$ steady-state crossflow separation condition. It will be noted that the peak level of this data (approximately 2.2 at a cross Mach Number near unity) agrees well with the very early data of Knowler and Pruden, shown in reference 12.

## D. BODY BASE INFLUENCE

The factor $k_2$ which was arbitrarily inserted into equation 6 and 7 is meant to account, in a crude fashion, for the effect of the body base on the crossflow normal force distribution.

Since the influence of the slender body nose has been accounted for via the crossflow drag impulsive flow analogy, the factor $k_2$ differs in nature from a similar factor used by Allen (1) to correct for three-dimensional crossflow effects at both the nose and ~~body~~ base of the body.

Reference 12 shows that this "end" effect has a negligible influence on the crossflow drag coefficient in supersonic flows, for cylinders of fineness ratio as low as four. However, at subsonic Mach numbers the "end" effects are significant. If it is assumed that each end of a finite-length circular cylinder has the effect of uniformly influencing the pressure level over the entire body length, and that the two end effects are additive, then the results of figure 8 in reference 12 can be used to estimate the factor $k_2$ for subsonic flows. Our factor $k_2$, which is the influence of only one "end" (the body base), will thus be equal to half the factor $\eta$ given in the above-quoted reference. A plot of the factor $k_2$ versus effective body fineness ratio is given in figure 7. The effective fineness ratio is given by

$$(16) \quad \frac{l_e}{d_b} = \frac{S_p}{d_b^2}$$

where $S_p$ is the planform (side) area of the body and $d_b$ is the base diameter.

## E. Comparison of Theory with Experiment

Since comparisons of gross experimental body normal force and pitching moment coefficients with theoretical calculations have lead previous investigators to erroneous conclusions concerning the accuracy of methods used in estimating the non-linear component of normal force and pitching moment, comparisons herein will be made only with local normal force distribution data. Such comparisons permit a determination not only of the gross normal force and pitching moment coefficients, but more important, the distribution of the normal force over the length of the body. Thus compensating errors which may be present in the theoretical calculations will be evident when comparing local theoretical normal force distributions with experimental distributions.

Unfortunately, only very limited unclassified local normal force distribution data is available. Such data is usually obtained by integrating pressure coefficient data around the circumference of the body at many axial locations. Such tests are time consuming and laborious to analyze. At subsonic speeds no suitable experimental normal force distribution data could be located. The gross normal force and pitching moment data presented in reference 7 served as a guide in formulating the theory presented.

At supersonic speed the data of references 3 and 4 provide some comparisons with the theory presented. Since the steady state crossflow drag coefficient data for supersonic speeds (at subsonic crossflow Mach numbers) was obtained from the data of reference 3, comparisons with the local normal force distributions of reference 3 would necessarily be quite good, but rather meaningless. Therefore, only the data of reference 4 is compared herein.

Figures 8,9,10 and 11 show the experimental normal force distributions of reference 4, at angles of attack of 5, 10, 15 and 20 degrees respectively. Both the linear and non-linear components of the calculated local normal force distribution are indicated in these figures. The sum of the linear and non-linear components, as given by equation 17, is to be compared with the experimental data indicated.

$$(17) \qquad C_n = C_{n_p} + C_{n_v} = (C_{n_\alpha})_p \sin\alpha\cos\alpha + C_{n_v}$$

The term $C_{n_v}$ is the viscous non-linear contribution as given by equation (5) and evaluated according to the method presented herein. Since it is desired to compare the non-linear viscous component of equation (17) with the experimental data shown, the linear component of equation (17) was extracted from the experimental data at an angle of attack of five degrees, for values of $\frac{x}{d_c} < 2.5$. Downstream of this station the theoretical values of Tsien, as given in figure 7 of reference 4, were used for the linear normal force coefficient distribution. It was felt that this approach gave the best estimate for the local linear normal force component, since crossflow separation commenced downstream of the station $\frac{x}{d_c} = 2.5$ at five degrees angle of attack.

Fortunately the experimental data of reference 4 were obtained at two different tunnel unit Reynolds numbers, between which the boundary layer over the body undergoes transition. The data in figure 9, at ten degrees angle of attack, shows the striking sensitivity of the non-linear crossforce to boundary layer condition. At a unit Reynolds number of $0.13(10)^6$ per inch the boundary layer appears to be totally laminar over the entire body length, and good agreement of experiment with the theory presented herein is indicated(note the poor agreement of the normal force distributions given by the theories of references 1 and 2, as obtained from

reference 4). However, at a unit Reynolds number of 0.39 $(10)^6$ per inch the boundary layer at $\alpha = 10$ degrees appeared to undergo transition at station $\frac{x}{d_c} \approx 3.5$ . The subsequent decrease in the non-linear normal force level is most significant and no theory is yet available which accurately predicts either the onset of this phenomenon, or its magnitude.

At an angle of attack of five degrees data was available only at the higher unit Reynolds number, shown in figure 8. Again boundary layer transition is observed to occur at a longitudinal station of $\frac{x}{d_c} \approx 5$ . Up to this station the agreement of the experimental data with the laminar crossflow theory derived herein is quite good.

At fifteen degrees angle of attack experimental data is again available at both unit Reynolds numbers, shown in figure 10. However, even at the lower unit Reynolds numbers of 0.13 $(10)^6$ per inch, the boundary layer appears to undergo transition at $\frac{x}{d_c} \approx 5.5$ . Up to this station the experimental and theoretical distributions agree quite well. At the higher unit Reynolds number with turbulence grid installed, transition appears to have occurred over nearly the entire body length.

At the highest angle of attack of twenty degrees for the experimental data of reference 4, only the higher unit Reynolds number was available. This experimental data is lower than the theoretical results of the method herein. However, this result is not unexpected since the boundary layer over the entire body was most likely in a transitional state at twenty degrees angle of attack. This condition is suggested by the trend of the experimental data at lower angles of attack.

The theoretical body station at which crossflow separation is assumed to occur, as given by equation (11), is indicated for each angle of attack

in figures 8 thru 11. It will be noted that this theoretical location appears to be somewhat too far upstream, as was expected. As a result the theoretical local normal force distribution between stations $X_5$ and $X_M$ (station $\frac{X_M}{d_c} \approx 5.75$ for the conditions of reference 4) is generally higher than the experimental distribution between these stations. This discrepancy does not appear to be extremely serious, though a more sophisticated criterion than equation (11) would represent an obvious improvement to the theoretical method presented here.

## F. Conclusions

As compared with laminar crossflow, it is noted that transitional or turbulent boundary layer crossflow separation produces significant changes in the local normal force distribution, with a generally lower level of crossflow drag. The laminar crossflow theory is not applicable to a transitional or turbulent boundary layer, even if lower crossflow drag coefficient levels are substituted for the laminar values predicted herein, since the steady-state turbulent crossflow drag coefficient is a strong function of angle of attack (reference 5 and 13).

For the case of totally laminar crossflow separation at supersonic speeds the method presented herein appears to produce good agreement with experiment for the prediction of normal force and pitching moment coefficients. A better criterion than equation (11) for the estimation of the onset of laminar crossflow separation should permit even closer agreement between theory and experiment.

## References:


1. NACA RM A 9126 Nov. 1949, H.J. Allen, "Estimation of the Forces and Moments Acting on Inclined Bodies of Revolution of High Fineness Ratio".

2. JAS August 1954, H.R. Kelly, "The Estimation of Normal Force, Drag, and Pitching-Moment Coefficients for Blunt-Based Bodies of Revolution at Large Angles of Attack".

3. NACA TN 3715, May 1956, E.W.Perkins and D.M. Kuehn, "Comparison of the Experimental and Theoretical Distributions of Lift on a Slender Inclined Body of Revolution at M=2".

4. NACA TN 3716, May 1956, E.W. Perkins and L.H. Jorgensen, "Comparison of Experimental and Theoretical Normal-Force Distributions (Including Reynolds Number Effects) on an Ogive - Cylinder Body at Mach Number 1.98"

5. NACA TN 2463, Sept. 1951, W.J. Burnsnall and L.K. Loftin, Jr. "Experimental Investigation of the Pressure Distribution about a Yawed Circular Cylinder in the Critical Reynolds Number Range."

6. AIAA Journal, Vol.4, No. 3, March 1966, T, Sarpkaya, "Separated Flow About Lifting Bodies and Impulsive Flow About Cylinders."

7. NACA RM A 51C14, May 1951, E.J. Hopkins, "A Semiempirical Method for Calculating the Pitching Moment of Bodies of Revolution at Low Mach Numbers."

8. NACA TM 1039, 1943, M.Schwabe, "Pressure Distribution in Nonuniform Two-Dimensional Flow."

## References


9. AIAA Journal, Vol. 4, No. 3, March 1966, T. Sarpkaya, " Separated Flow About Lifting Bodies and Impulsive Flow About Cylinders."

10. Journal of the Aeronautical Sciences, Vol. 18 No. 3, March 1951, M.D. Van Dyke, "First and Second-Order Theory of Supersonic Flow Past Bodies of Revolution."

11. Journal of the Aeronautical Sciences, Vol.5 No. 12, Oct. 1938, H.S. Tsien, "Supersonic Flow Over an Inclined Body of Revolution."

12. NACA TN 2960, June 1953, F.E. Goven and E.W. Perkins, " Drag of Circular Cylinder for a Wide Range of Reynolds numbers and Mach numbers."

13. Fluid Dynamic Drag, S.F. Hoerner

14. U.S.A.F. Stability and Control Datcom, Oct. 1960, revised Nov. 1965

15. Journal of the Aeronautical Sciences, Vol. 17 No. 11, Nov. 1950, G. Grimminger, E.P.Williams and G.B. Young, "Lift on Inclined Bodies of Revolution in Hypersonic Flow."

FIGURE 1

GEOMETRY OF BODY OF REVOLUTION AT ANGLE OF ATTACK, $\alpha$

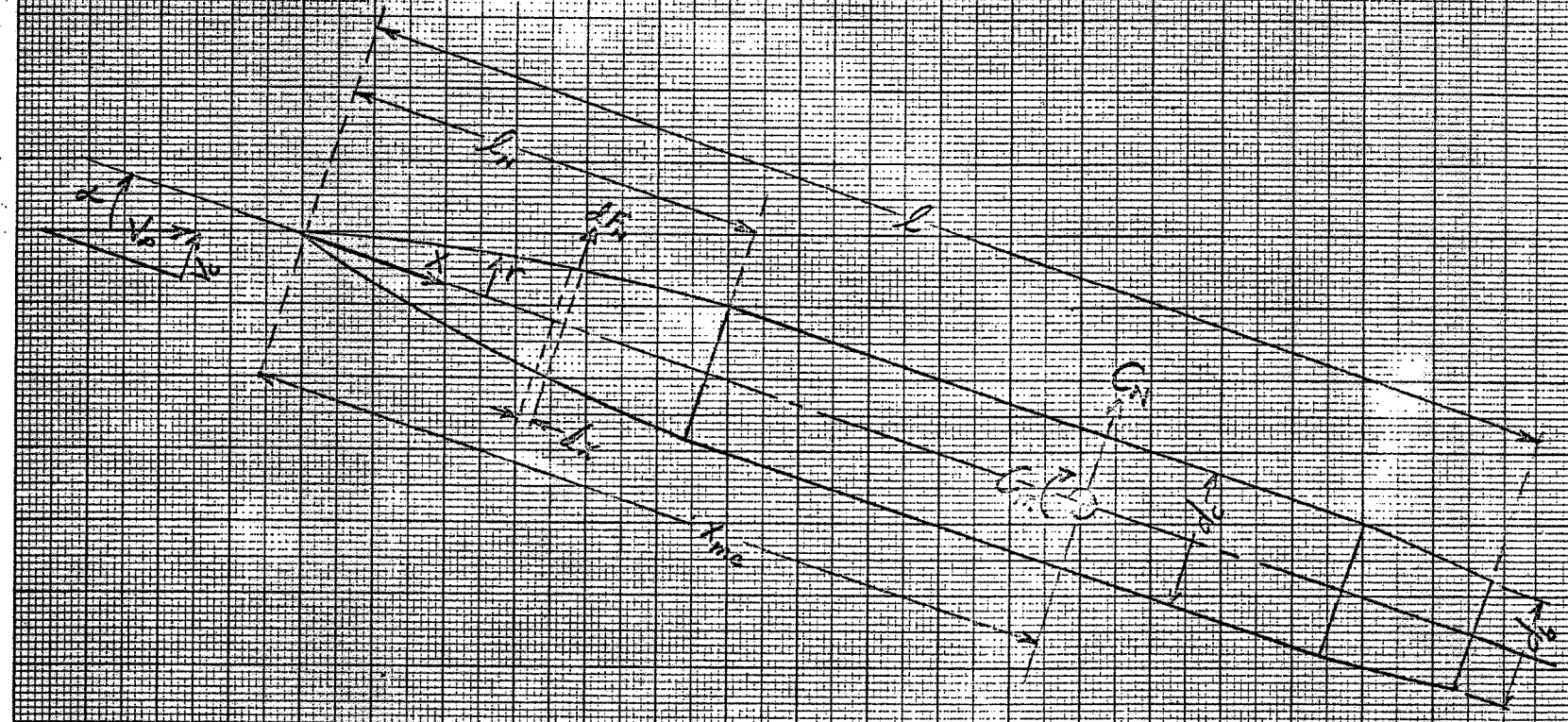

FIGURE 2

AXIAL DISTRIBUTION OF LAMINAR CROSSFLOW DRAG COEFFICIENT RATIO

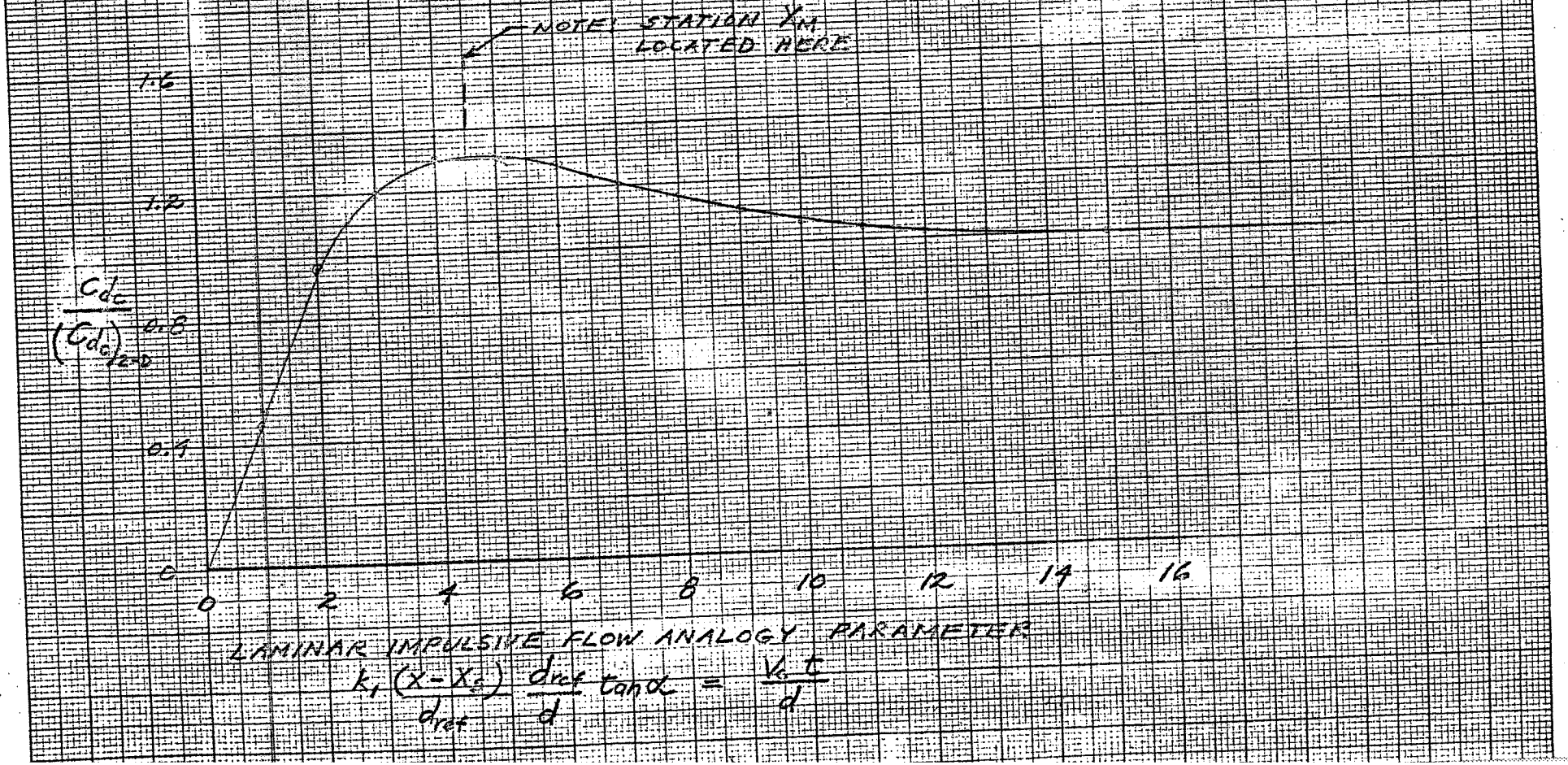

FIGURE 5

APPROXIMATE POSITION OF MINIMUM IN DISTRIBUTION OF POTENTIAL FLOW LOCAL NORMAL FORCE COEFFICIENT DISTRIBUTION (STATION $X_M$)

$5° \leq \theta_v \leq 15°$

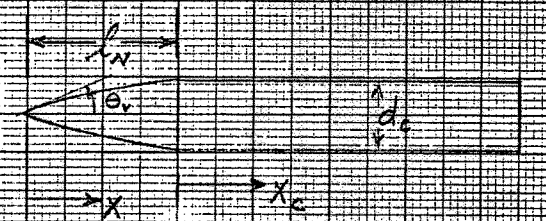


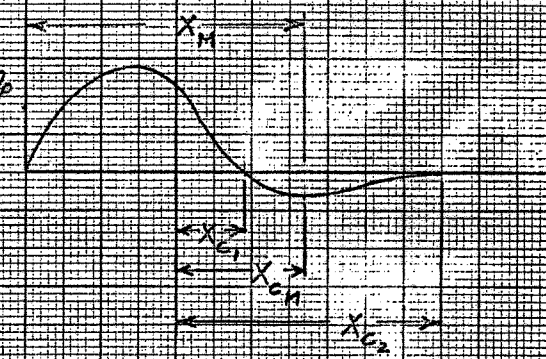


$X_M = X_{c_M} + l_N$

$l_N$ = NOSE LENGTH
$d_c$ = CYLINDER DIAMETER

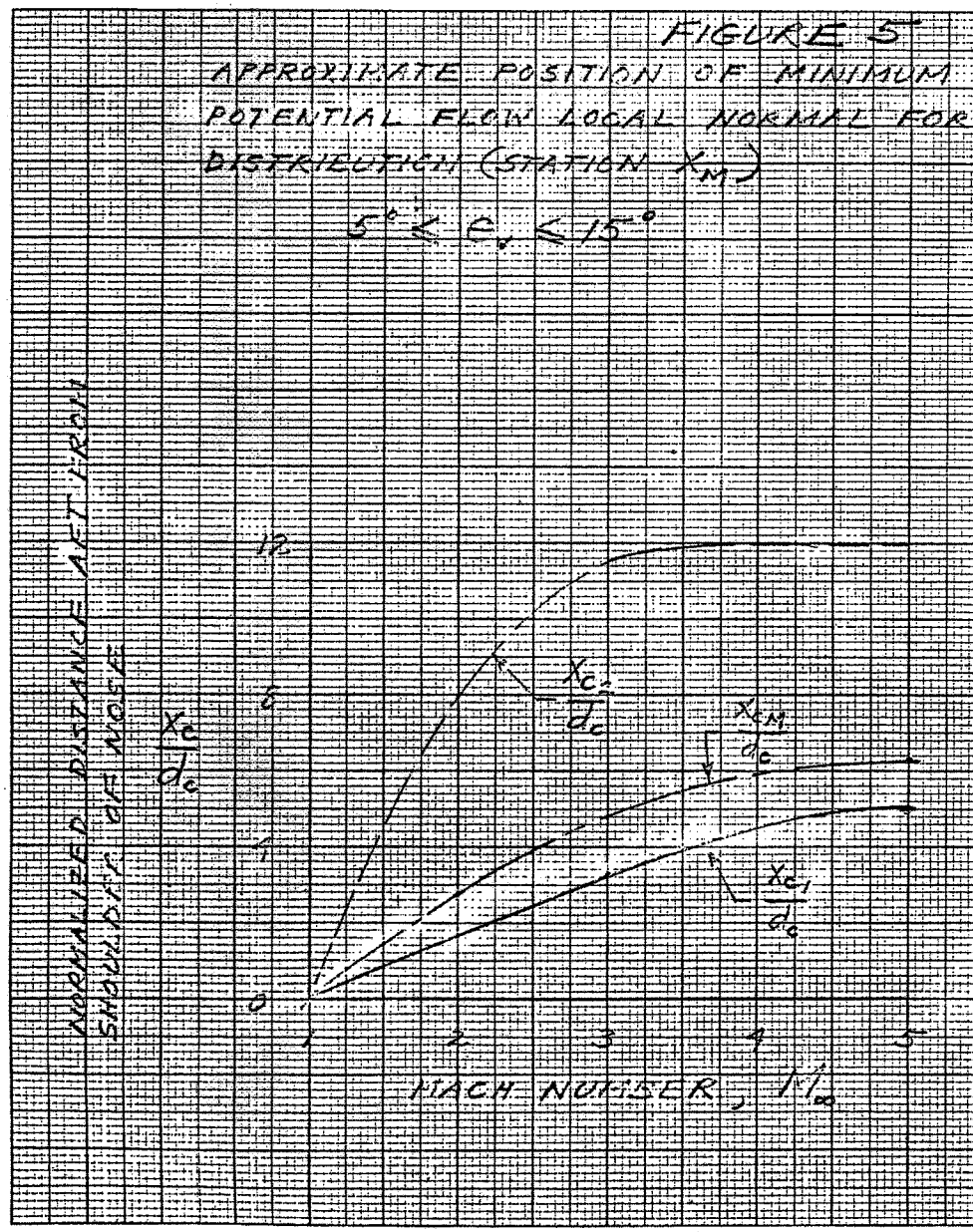

# FIGURE 6

## TWO-DIMENSIONAL, STEADY STATE CROSSFLOW DRAG COEFFICIENT VERSUS CROSSFLOW MACH NUMBER (LAMINAR BOUNDARY LAYER)

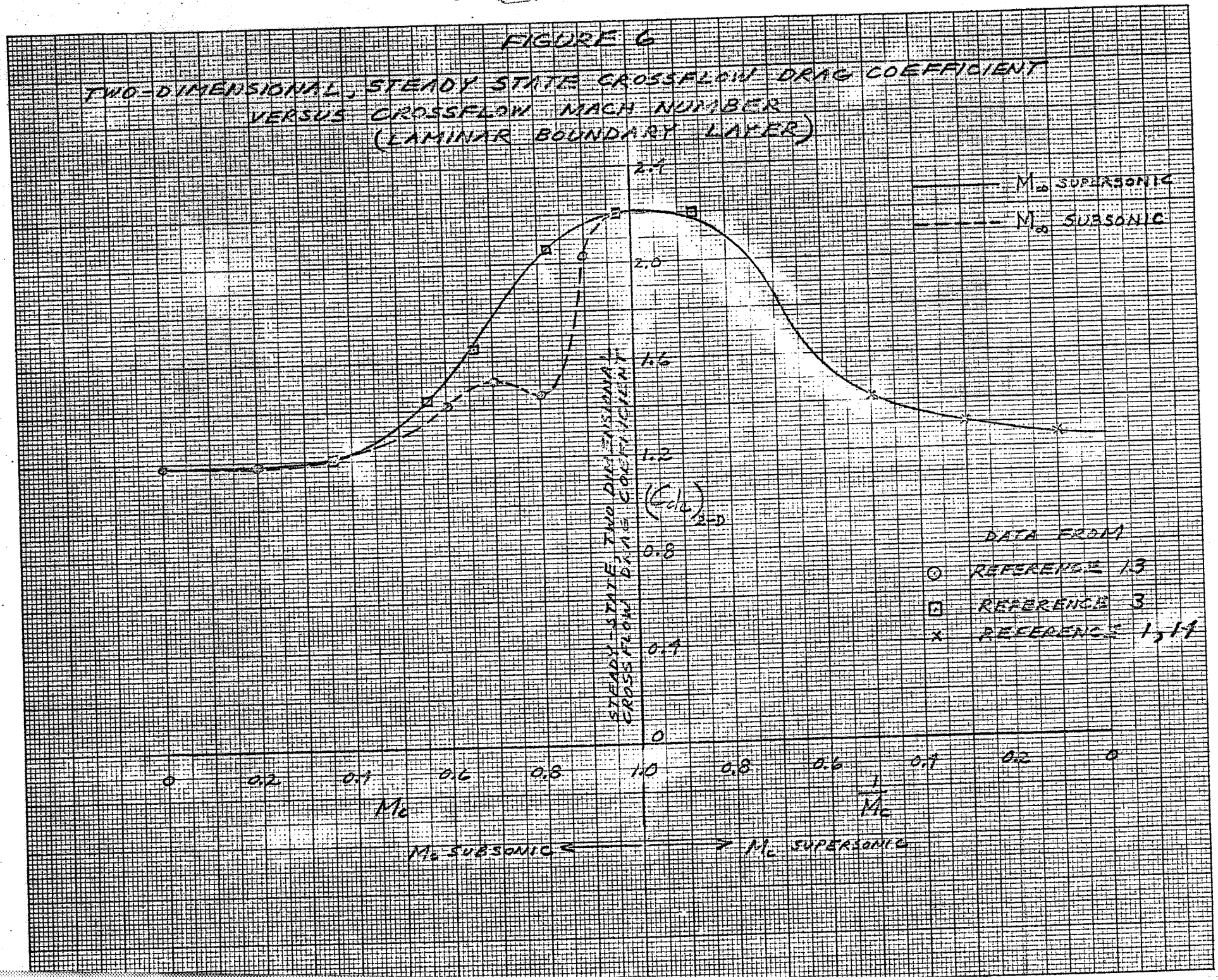

FIGURE 7

BODY BASE INFLUENCE ON CROSSFLOW DRAG COEFFICIENT

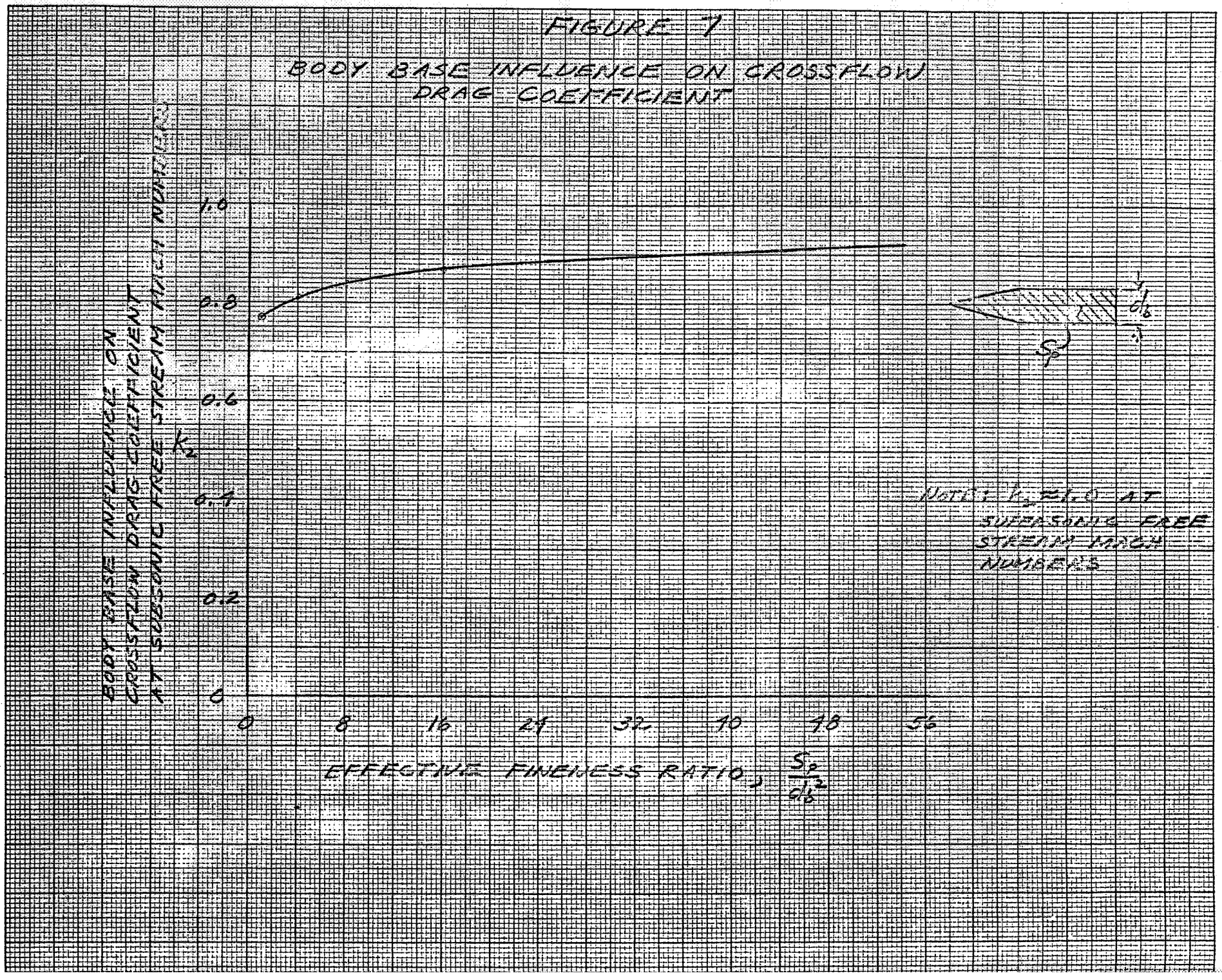

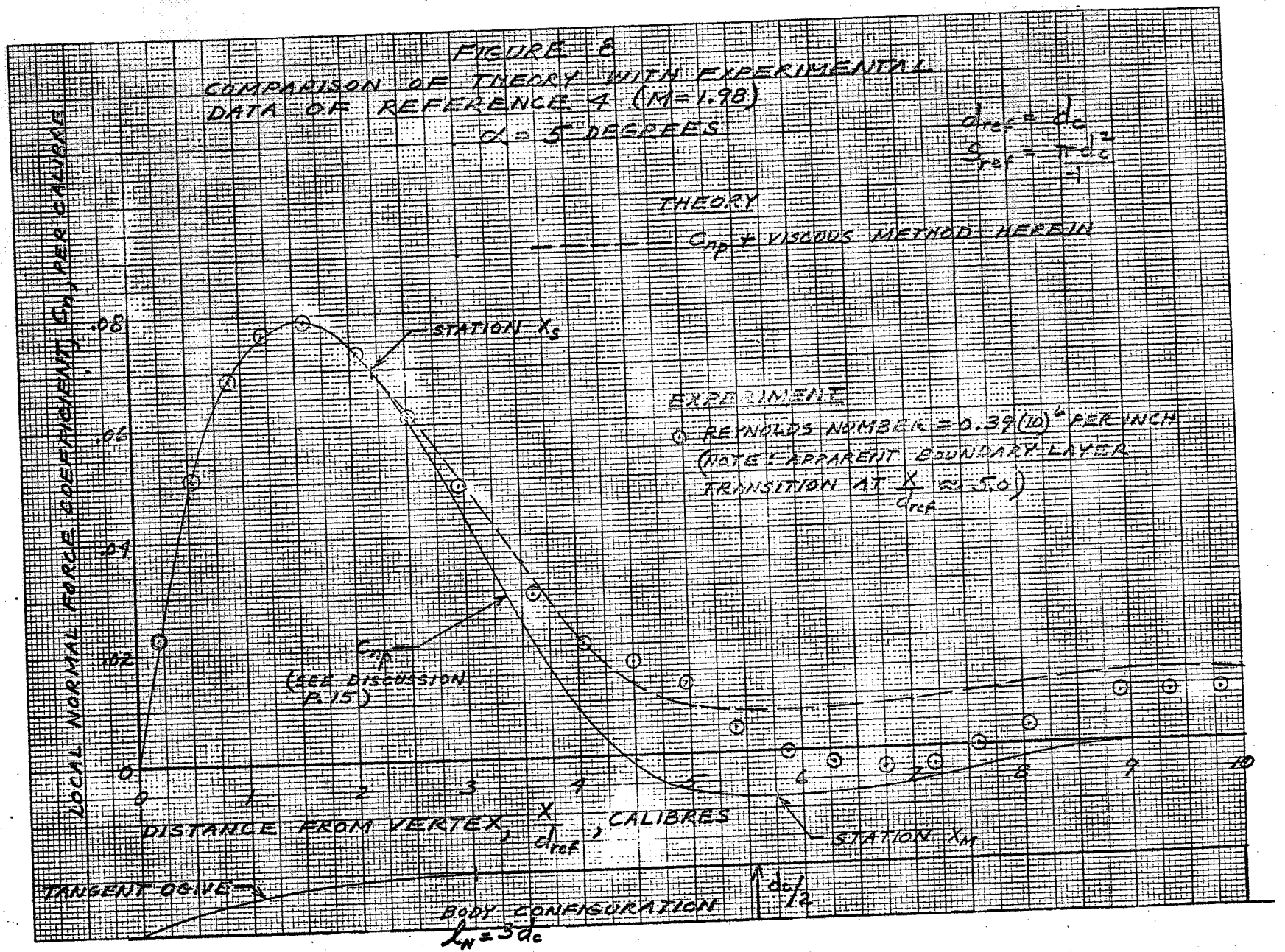
FIGURE 8
COMPARISON OF THEORY WITH EXPERIMENTAL DATA OF REFERENCE 4 (M=1.98)
α = 5° DEGREES
$d_{ref} = d_c$
$S_{ref} = \pi \frac{d_c^2}{4}$
THEORY
$C_{np}$ + VISCOUS METHOD HEREIN
EXPERIMENT
REYNOLDS NUMBER = 0.39(10)⁶ PER INCH
(NOTE: APPARENT BOUNDARY LAYER TRANSITION AT $\frac{X}{C_{ref}} \approx 5.0$)
STATION $X_S$
STATION $X_M$
$C_{np}$
(SEE DISCUSSION P. 15)
LOCAL NORMAL FORCE COEFFICIENT, $C_n$, PER CALIBRE
.08
.06
.04
.02
0
0
1
2
3
4
5
6
7
8
9
10
DISTANCE FROM VERTEX, $\frac{X}{d_{ref}}$, CALIBRES
TANGENT OGIVE
BODY CONFIGURATION
$l_N = 3d_c$
$d_c/2$

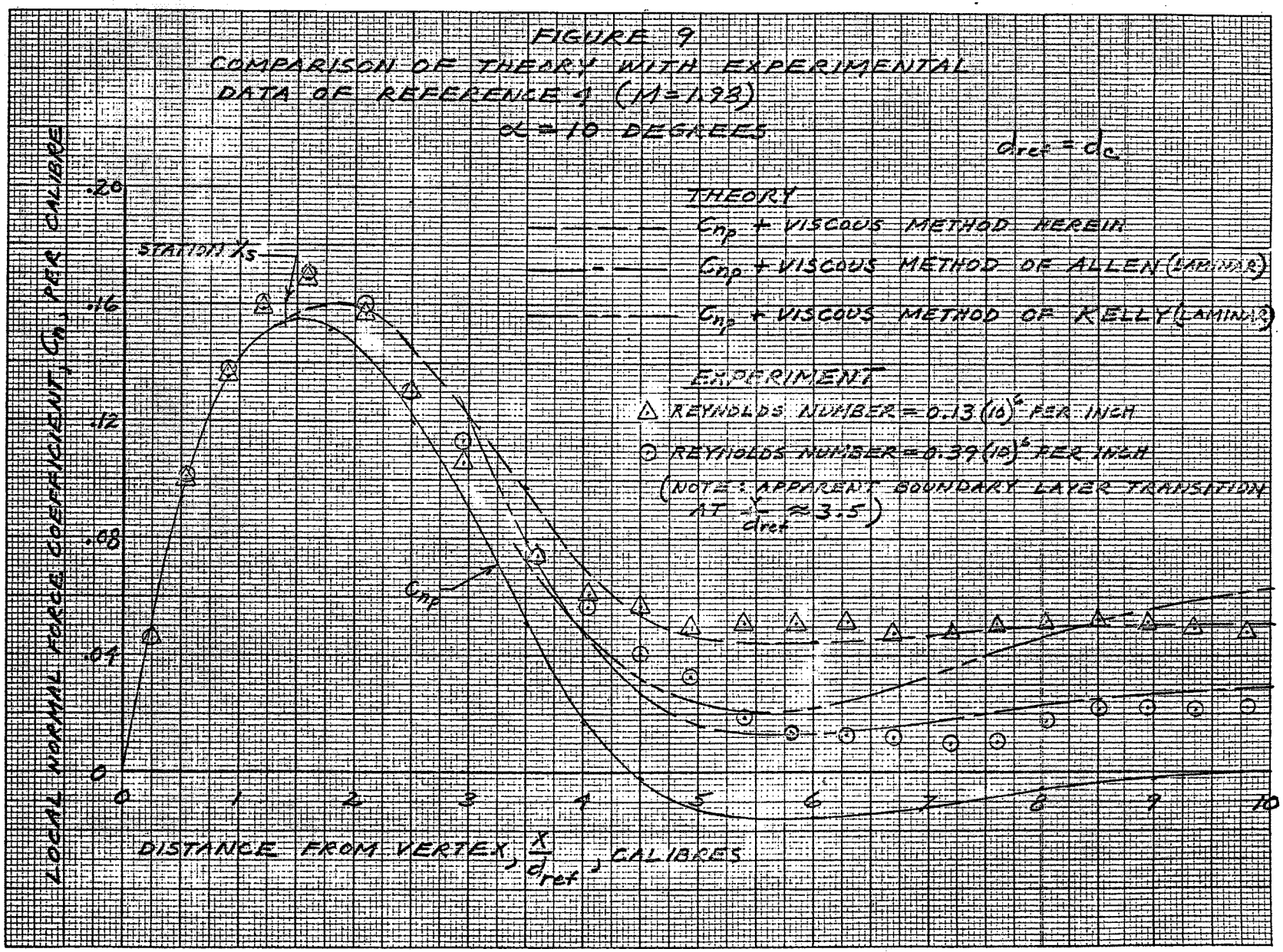
FIGURE 9
COMPARISON OF THEORY WITH EXPERIMENTAL DATA OF REFERENCE 4 (M=1.93)
α = 10 DEGREES
$d_{ref} = d_c$
THEORY
$C_{n_p}$ + VISCOUS METHOD HEREIN
$C_{n_p}$ + VISCOUS METHOD OF ALLEN (LAMINAR)
$C_{n_p}$ + VISCOUS METHOD OF KELLY (LAMINAR)
EXPERIMENT
△ REYNOLDS NUMBER = 0.13 (10)⁶ PER INCH
○ REYNOLDS NUMBER = 0.39 (10)⁶ PER INCH
(NOTE: APPARENT BOUNDARY LAYER TRANSITION AT $\frac{x}{d_{ref}} \approx 3.5$)
STATION $x_s$
$C_{n_p}$
LOCAL NORMAL FORCE COEFFICIENT $C_n$ PER CALIBRE
.20
.16
.12
.08
.04
0
0
1
2
3
4
5
6
7
8
9
10
DISTANCE FROM VERTEX, $\frac{x}{d_{ref}}$, CALIBRES

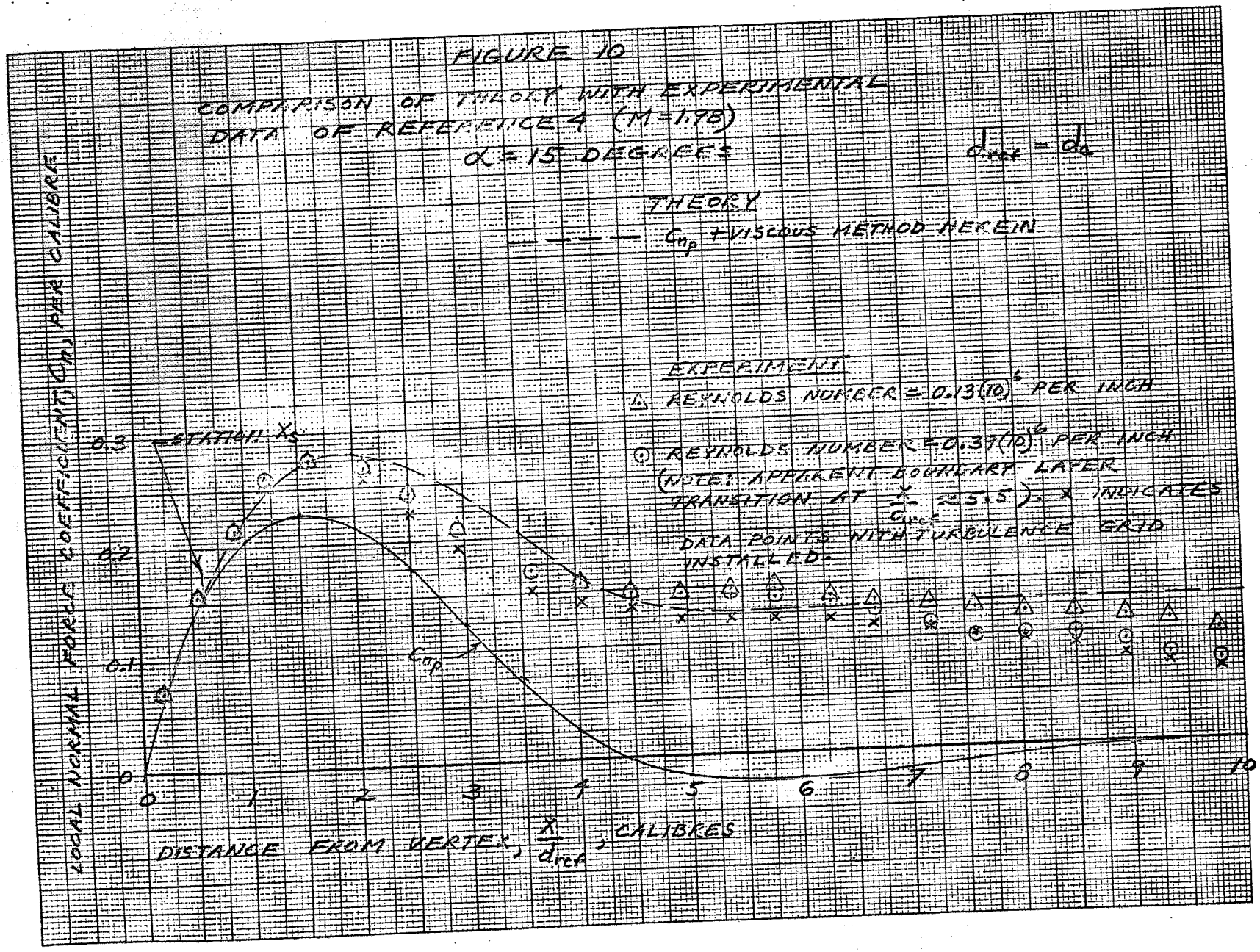
FIGURE 10
COMPARISON OF THEORY WITH EXPERIMENTAL DATA OF REFERENCE 4 (M=1.98)
α = 15 DEGREES
$d_{ref} = d_c$
THEORY
$C_{n_p}$ + VISCOUS METHOD HERCEIN
EXPERIMENT
△ REYNOLDS NUMBER = 0.13(10)$^6$ PER INCH
⊙ REYNOLDS NUMBER = 0.37(10)$^6$ PER INCH
(NOTE: APPARENT BOUNDARY LAYER TRANSITION AT $\frac{x}{c_{ref}}$ = 5.5). X INDICATES DATA POINTS WITH TURBULENCE GRID INSTALLED.
STATION: $X_S$
LOCAL NORMAL FORCE COEFFICIENT ($C_N$) PER CALIBER
$C_{n_p}$
0.3
0.2
0.1
0
0
1
2
3
4
5
6
7
8
9
10
DISTANCE FROM VERTEX, $\frac{x}{d_{ref}}$, CALIBERS

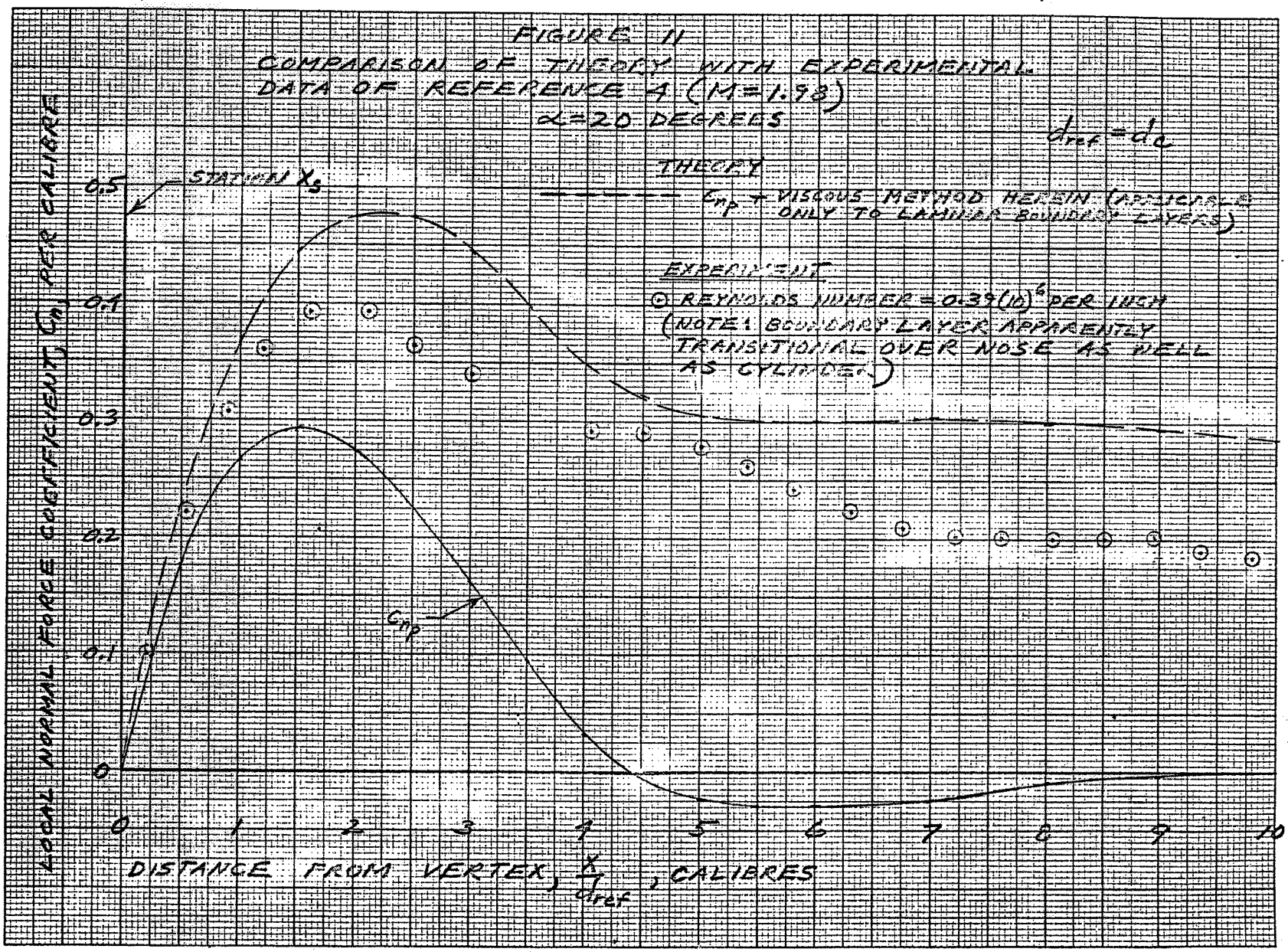
FIGURE 11
COMPARISON OF THEORY WITH EXPERIMENTAL DATA OF REFERENCE 4 (M=1.98)
α=20 DEGREES
$d_{ref} = d_c$
THEORY
$C_{np}$ + VISCOUS METHOD HERE IN (APPLICABLE ONLY TO LAMINAR BOUNDARY LAYERS)
EXPERIMENT
⊙ REYNOLDS NUMBER = 0.39(10)$^6$ PER INCH
(NOTE: BOUNDARY LAYER APPARENTLY TRANSITIONAL OVER NOSE AS WELL AS CYLINDER)
STATION $X_s$
$C_{np}$
LOCAL NORMAL FORCE COEFFICIENT ($C_n$) PER CALIBRE
0.5
0.4
0.3
0.2
0.1
0
0
1
2
3
4
5
6
7
8
9
10
DISTANCE FROM VERTEX, $\frac{X}{d_{ref}}$, CALIBRES